This document is the accepted manuscript version of the following article:
Nango, E., Royant, A., Kubo, M., Nakane, T., Wickstrand, C., Kimura, T., … Iwata, S. (2016). A three-dimensional movie of structural changes in bacteriorhodopsin. Science, 354(6319), 1552-1557. https://doi.org/10.1126/science.aaH3497

A THREE DIMENSIONAL MOVIE OF STRUCTURAL CHANGES IN BACTERIORHODOPSIN

Eriko Nango,[1,2] Antoine Royant,[3,4 †] Minoru Kubo,[1,5 †] Takanori Nakane,[6] Cecilia Wickstrand,[7] Tetsunari Kimura,[1,8] Tomoyuki Tanaka,[1] Kensuke Tono,[9] Changyong Song,[1,10] Rie Tanaka,[1] Toshi Arima,[1] Ayumi Yamashita,[1] Jun Kobayashi,[1] Toshiaki Hosaka,[11] Eiichi Mizohata,[12] Przemyslaw Nogly,[13] Michihiro Sugahara,[1] Daewoong Nam,[10] Takashi Nomura,[1] Tatsuro Shimamura,[2] Dohyun Im,[2] Takaaki Fujiwara,[2] Yasuaki Yamanaka,[2] Byeonghyun Jeon,[10] Tomohiro Nishizawa,[5,6] Kazumasa Oda,[6] Masahiro Fukuda,[6] Rebecka Andersson,[7] Petra Båth,[7] Robert Dods,[7] Jan Davidsson,[14] Shigeru Matsuoka,[15] Satoshi Kawatake,[15] Michio Murata,[15] Osamu Nureki,[6] Shigeki Owada,[1] Takashi Kameshima,[9] Takaki Hatsui,[1] Yasumasa Joti,[9] Gebhard Schertler,[13,16] Makina Yabashi,[1] Ana-Nicoleta Bondar,[17] Jörg Standfuss,[13] Richard Neutze,[7 ‡] So Iwata [1,2 ‡]

[1] RIKEN SPring-8 Center, 1-1-1 Kouto, Sayo-cho, Sayo-gun, Hyogo 679-5148, Japan.

[2] Department of Cell Biology, Graduate School of Medicine, Kyoto University, Yoshidakonoe-cho, Sakyo-ku, Kyoto, 606-8501, Japan.

[3] Université Grenoble Alpes, CNRS, CEA, Institut de Biologie Structurale, F-38044 Grenoble,

France.

[4] European Synchrotron Radiation Facility, F-38043 Grenoble, France.

[5] JST–PRESTO, 4-1-8 Honcho, Kawaguchi, Saitama 332-0012, Japan.

[6] Department of Biological Sciences, Graduate School of Science, University of Tokyo, 2-11-16 Yayoi, Bunkyo-ku, Tokyo 113-0032, Japan.

[7] Department of Chemistry and Molecular Biology, University of Gothenburg, Box 462, SE-40530 Gothenburg, Sweden.

[8] Department of Chemistry, Graduate School of Science, Kobe University, 1-1 Rokkodai, Nada-ku, Kobe 657-8501, Japan.

[9] Japan Synchrotron Radiation Research Institute, 1-1-1, Kouto, Sayo-cho, Sayo-gun, Hyogo 679-5198, Japan.

[10] Department of Physics, Pohang University of Science and Technology, Pohang 790-784, Korea.

[11] Division of Structural and Synthetic Biology, RIKEN Center for Life Science Technologies, 1-7-22 Suehiro-cho, Tsurumi-ku, Yokohama 230-0045, Japan.

[12] Department of Applied Chemistry, Graduate School of Engineering, Osaka University, 2-1 Yamadaoka, Suita, Osaka 565-0871, Japan.

[13] Division of Biology and Chemistry - Laboratory for Biomolecular Research, Paul Scherrer Institute, 5232 Villigen, Switzerland.

[14] Department of Chemistry-Ångström Laboratory, Uppsala University, Uppsala, Sweden.

[15] JST–ERATO, Lipid Active Structure Project, Osaka University, 1-1 Machikaneyama, Toyonaka, Osaka 560-0043, Japan.

[16] Department of Biology, ETH Zurich, 8093 Zürich, Switzerland

[17] Theoretical Molecular Biophysics, Department of Physics, Freie Universitaet Berlin, Arnimallee 14, D-14195 Berlin, Germany.

[†] These authors contributed equally to this study.

[‡] To whom correspondence should be addressed. E-mail: richard.neutze@gu.se or s.iwata@spring8.or.jp

One sentence summary: Time-resolved serial crystallography at an X-ray free electron laser reveals structural changes in bacteriorhodopsin.

ABSTRACT

Bacteriorhodopsin (bR) is a light-driven proton pump and a model membrane transport protein. Here we use time-resolved serial femtosecond crystallography at an X-ray free electron laser to visualize conformational changes in bR from nanoseconds to milliseconds following photoactivation. An initially twisted retinal chromophore displaces a conserved tryptophan residue of transmembrane helix F on the cytoplasmic side of the protein while dislodging a key water molecule on the extracellular side. The resulting cascade of structural changes throughout the protein show how motions are choreographed as bR transports protons uphill against a transmembrane concentration gradient.

Energy coupled membrane transport proteins are ubiquitous in biology. The basic framework underpinning unidirectional membrane transport is called the *alternating access model* and was proposed by Jardetzky half a century ago (*1*). This theory postulates that a high-affinity binding site which is initially accessible to one side of the membrane is converted through structural changes into a low-affinity binding site that is accessible to the other side of the membrane (fig. S1). The recent advent of time-resolved serial femtosecond crystallography (TR-SFX) at an X-ray free electron laser (XFEL) (*2-4*) provides an opportunity to examine this framework.

Bacteriorhodopsin (bR) harvests the energy content of light to drive conformational changes leading to unidirectional proton transport. Energy stored within a transmembrane proton concentration gradient is converted by ATP-synthase into ATP or is coupled to other transport processes. Considerable effort has been made to understand how structural changes in bR transport a proton uphill against a transmembrane potential (*5-7*). Crystallographic structures derived from data recorded at cryogenic temperature reveal both light and mutation-induced structural changes in bR (*6*, *7*) but this work is controversial because the reported structures show considerable variation (*7*), structures trapped at cryogenic temperature or by mutation do not correlate directly with time-dependent structural changes in wild-type bR, and it is argued that X-ray induced radiation damage may mislead the interpretation of trapped intermediate structures (*8-10*). Here we circumvent these concerns by recording a 3D movie of structural changes in bR at room-temperature at 2.1 Å resolution using TR-SFX (*2-4*). The principle of "diffraction before destruction" (*11*) ensures that crystallographic structures are effectively free from the influence of X-ray induced radiation damage (*12*) using 10 fs long XFEL pulses at the SPring-8 Angstrom Compact Free Electron Laser (SACLA).

Structure of the bR resting conformation

bR is a seven transmembrane α-helix protein containing a buried *all-trans* retinal chromophore that is covalently attached through a protonated Schiff base (SB) to Lys216 of helix G. Light photo-excites the chromophore which isomerizes with high quantum yield to a 13-*cis* configuration (Fig. 1A) and thereby initiates a sequence of spectral (fig. S2) and structural changes that facilitate spontaneous proton exchange between acidic and basic amino acid residues (Fig. 1B). Electron density for the resting state bR structure (Fig. 1C, table S1) shows how the protonated SB forms a H-bond interaction to Wat402 (*13*) which is critical for attaining the remarkably high SB proton affinity with a pKa of 13.3 (*14*). Asp85, the primary proton acceptor, also forms a H-bond interaction with Wat402 and additional H-bond interactions with Thr89 and Wat401 ensure its low resting state pKa of 2.2 (*15*). A difference of eleven orders of magnitude between the proton affinities of the primary donor and acceptor prevents the leakage of protons from the extracellular (EC) medium to the cytoplasm (CP) but raises the question of what brings these proton affinities close together in order to facilitate spontaneous proton exchange? It is also puzzling why it takes microseconds for the primary proton transfer to occur when the SB and Asp85 are initially separated by only 4 Å and a water mediated proton exchange pathway between these two groups is seen in the resting state (*13*). Moreover, protons are pumped from the CP to the EC yet retinal isomerization redirects the SB proton away from the EC and towards the CP (Fig. 1A), which appears to contradict Jardetzky's framework.

Time-resolved spectroscopy studies of bR microcrystals

Photoactivated bR progresses through a sequence of spectral intermediates labeled K, L, M_1 (early M), M_2 (late M), N and O prior to returning to the bR resting state (fig. S2). A proton is transferred from the SB to Asp85 in the L to M transition and from Asp96 to the SB from M to N. Time-resolved difference absorption spectra from bR microcrystals suspended in a lipidic cubic phase (LCP) matrix (fig. S3A) show a photo-cycle turnover that is similar to that of wild-type bR in the purple membrane. Spectral decomposition reveals that for $\Delta t \leq 10$ μs the photoactivated population in microcrystals is dominated by the L intermediate but with traces of K, whereas the M-intermediate population increases to 50 % at $\Delta t = 19$ μs and falls to 50 % at $\Delta t = 9$ ms (fig. S3B,C). Measurements from four independent crystal batches give the half-rise for the M-state as 15 ± 7 μs and the half-decay as 8 ± 3 ms.

Overview of structural rearrangements within the bR photocycle

In TR-SFX a continuous stream of microcrystals are injected across a focused XFEL beam and the delay between sample photoactivation and the arrival of an XFEL pulse is controlled electronically (*2-4*) (fig. S4). TR-SFX data were recorded to 2.1 Å resolution from light-adapted bR microcrystals following photoactivation by a ns laser pulse for the time-delays Δt = 16 ns, 40 ns, 110 ns, 290 ns, 760 ns, 2 μs, 5.25 μs, 13.8 μs, 36.2 μs, 95.2 μs, 250 μs, 657 μs and 1.725 ms (table S1), which are evenly spaced on a logarithmic scale. A global overview of the evolution of difference electron density reveals how structural changes first emerge near the active site of the protein and become stronger around Lys216 of helix G and Trp182 of helix F prior to cascading towards the EC side of the protein along helix C (fig. S5; Movie S1).

Early structural changes in the bR photocycle

For Δt = 16 ns, which corresponds to essentially pure K-intermediate, paired negative and positive difference electron density features adjacent to the C20 methyl group reveal that the retinal is initially tilted towards helix G in response to photo-isomerization (Fig. 2A). Combined quantum mechanics and molecular mechanics computations also favor a twisted retinal geometry (fig. S6) and indicate that approximately 17 kcal/mol of energy is initially stored within this distorted active site configuration, which equates to 32 % of the absorbed photon's energy and is compatible with earlier estimates (*16, 17*). By Δt = 290 ns the positive difference density feature associated with the C20 methyl is much weaker and moves into the plane of the retinal whereas paired negative and positive difference electron density features associated with Trp182 grow stronger (Fig. 2B), showing how Trp182 is displaced towards the CP as the retinal straightens (Fig. 2C). Negative and positive difference electron density features also indicate a movement of the side-chain and backbone of Lys216 has begun at Δt = 16 ns (Movies S2-3).

A strong negative difference electron density peak visible at Δt = 16 ns on Wat402 (Fig. 2A) shows that this water molecule is rapidly disordered by retinal isomerization. This feature doubles in strength as the photocycle evolves (Fig. 3A, Movies S2-3, table S2) from which we infer that the freedom of Wat402 to move is initially constrained by the limited size of the cavity in which it is buried, yet this water becomes increasingly mobile as the retinal is displaced towards the CP. Low-temperature trapping studies have suggested that Wat402 disorders upon retinal photo-isomerization (*18*) but this conclusion was challenged in light of similar observations due to X-ray induced radiation damage (*8-10*). Because no effects of radiation damage are visible when using XFEL pulses ≤ 10 fs in duration at an X-ray dose of 12 MGy (*12, 19*) these TR-SFX data bring closure to this debate. It is noteworthy that one trapped K-intermediate showed Wat402 disordering (*18*) but did not visualize a twist of the retinal C20 methyl towards helix G (Fig. 2A,C) whereas another captured this twist but kept Wat402 in the K-state model (*8*) and a third K-state structure showed neither change (*20*).

Conformational changes associated with proton transfer

The key step in achieving unidirectional proton transport by bR is the primary transfer event from the SB to Asp85 (the L-to-M transition) because only the mutation of Asp85 (*21*) or the removal of retinal completely stops proton pumping. Our data reveal a smooth evolution of electron density changes on the CP side of helix F and G prior to proton transfer (Fig. 3B, Movies S1, S3). Paired positive and negative density features also show that the side-chain of Leu93 is displaced towards the CP and a weaker positive difference electron density peak arises between the retinal, Leu93 and Thr89 from Δt = 40 ns until 13.8 μs (Fig. 4A) and is strongest at Δt = 760 ns (Fig. 3C, table S2). We modeled this feature as a transient water molecule (Wat452, Fig. 4B) which shows weak H-bond interactions with the SB (3.35 Å) and the backbone carbonyl oxygen of Thr89 (3.35 Å). Its crystallographic distance to Oγ of Thr89 of 3.95 Å may also be classified as a weak H-bond interaction (*22*). Structural refinement shows that for Δt = 16 ns, Oγ of Thr89 is separated from the SB by 3.97 Å and the SB nitrogen is pointing towards helix G, whereas for Δt = 760 ns the SB nitrogen rotates almost 180° towards helix C and reduces the SB-Oγ separation to 3.30 Å. Fluctuations about these crystallographic position could therefore create a transient proton-transport pathway linking the SB to Asp85 through Wat452 and Thr89 (Fig. 4B).

A water molecule was built at the Wat452 location in one cryo-trapped L-intermediate structure

(*23*) but was not observed in any other L-state study (*24-26*). FTIR spectroscopy observations have inferred that a transient H-bond interaction of the SB to a water molecule arises in the L-state (*27, 28*) and Wat452 is the only plausible candidate for this interaction. Computer simulations also establish that a water molecule at this position can channel a proton to Asp85 through Thr89 (*29*). Another transient water molecule (Wat453) which forms H-bond interactions with the carbonyl oxygen of Lys216 and the backbone nitrogen of Gly220 was also predicted from FTIR spectroscopy studies (*30*) and is observed in the difference electron density.

On the EC side of the retinal, the disordering of Wat402 triggers a structural cascade visible from $\Delta t \geq 13.8$ μs as significant ($\geq 4\sigma$) difference electron density peaks that show the disordering of Wat400 and Wat401 and the ordering of a new water molecule, Wat451, between Asp85 and Asp212 (Fig. 5, table S2).Concomitant with these active-site water rearrangements is an increase in the strength of paired negative and positive difference density features along the EC portions of helix C (residues 82 to 89, Fig. 3A) which are modeled as a concerted inwards movement of helix C towards helix G (Fig. 5C). These observations are similar to electron density changes recorded in low-temperature trapping studies of the bR L-state (*7, 24, 25*) but TR-SFX data show that this inwards flex of helix C approaches its maximum amplitude as the SB is deprotonated (*ie*. as the M-state population grows, Fig. 3A). Protons exchange between consecutive water molecules in the model channel gramicidin A on a sub-picosecond time-scale (*31*) and the primary proton transfer should be very fast once a structure facilitating this exchange is attained. Consequently the time required for bR to evolve to a conformation with helix C bent towards helix G is the rate limiting step that controls the primary proton transfer and explains why it takes microseconds for the SB to be deprotonated.

Breaking the EC connectivity after proton transfer

A key conceptual issue underpinning membrane transport is the nature of the “switch”, or more specifically how the SB breaks access to the EC side of bR after the primary proton transfer to Asp85. This is central to the mechanism of proton pumping because structural changes must prevent Asp85 from reprotonating the SB or otherwise the photocycle would be futile. A switch may be achieved by breaking the pathway for the reverse proton transfer, or by perturbing the chemical environment of key groups to shift the equilibrium in favor of the forward proton transfer reaction.

Difference electron density features associated with movements of the retinal, helix F (Trp182, Thr178 and Arg175) and helix G (Lys216, Ala215 and Ser214) all show a stepwise increase in strength from Δt = 5.25 μs to 36.2 μs, which coincides with the primary proton transfer event (Fig. 3B). We therefore conclude that proton transfer from the SB to Asp85 affects a structural change within the retinal which we model as a displacement of the SB towards the CP by 0.15

Å, and of the C20 methyl by 0.21 Å, over the interval 760 ns $\leq \Delta t \leq$ 36.2 μs. These changes may be due to the retinal being subtly straighter when deprotonated (*32*) or due to proton transfer neutralizing the mutual electrostatic attraction between the SB and Asp85 (*6*). Both geometric and electrostatic effects increase the separation between the SB and Asp85 and would therefore increase the barrier for the reverse proton transfer.

Protein structural changes also hinder the reverse proton transfer from Asp85 to the SB. Wat452, which may help mediate the primary proton transfer through Thr89 (Fig. 4B), is observed for 40 ns $\leq \Delta t \leq$ 13.8 μs but is not visible after a proton is transferred to Asp85 (Fig. 3C, table S2). An H-bond interaction connecting Thr89 to Asp85 is also lost after the primary proton transfer event, with significant ($\geq 4\ \sigma$) negative difference electron density becoming visible between Oγ of Thr89 and Oδ of Asp85 for $\Delta t \geq$ 36.2 μs (Fig. 5D, Movie S2, table S2). These structural changes break the reverse proton transfer pathway from Asp85 to the SB through Thr89 and Wat452 while simultaneously increasing the pKa of Asp85. Thr89 moves closer to the retinal in the M-state with the H-bond from Oγ of Thr89 to the SB decreasing from 3.30 Å at 760 ns to 3.04 Å at 36.2 μs and to 2.86 Å at 1.725 ms. This tighter H-bond donor interaction to the deprotonated SB locks Thr89 in a conformation that allows the Asp85 side chain to rotate and break its connectivity to Thr89 while forming a new H-bond interaction with Wat451. In contrast with TR-SFX, FTIR spectroscopy studies at low temperature have predicted a tight

Thr89-Asp85 H-bond interaction in the M-state (*33*), but the complex dynamics of these residue's H-bond interactions may preclude a unique interpretation of spectroscopic observations.

Synchronous with the M-state spectral transition is a displacement of the positively charged head group of Arg82 towards the EC (Figs. 3A, 5C), which implies that this movement is triggered by the protonation of Asp85. This rearrangement displaces a positive charge away from Asp85 and consequently increases the pKa of the primary proton acceptor, hindering the reverse proton transfer reaction (*34*). These structural perturbations also trigger a rearrangement of Glu194 and Glu204 which were modeled from $\Delta t \geq 250$ µs. Similar structural changes have been observed for trapped M-intermediates and were argued to influence the release of a proton to the EC medium (*34*, *35*). Overall, this sequence highlights structural changes that favor Asp85 being protonated and reveal how the SB accessibility to the EC side of the protein is broken after the SB is deprotonated, thereby functionally coupling the primary proton transfer event to the switch in the bR photocycle.

Structural changes on the CP side of bR

Correlated movements are observed on the CP side of helix F as paired negative and positive difference electron density stacking through Trp182, Thr178 and Arg175 (Fig. 6A,B; Movie

S3). As with electron density changes associated with the retinal and near the center of helix G, difference density features on CP portions of helix F arise rapidly but plateau once the SB is deprotonated (Fig. 3B). Structural refinement indicates that the retinal's C20 methyl group is displaced by 1.12 Å towards the CP over the time-sequence sampled here, with a corresponding displacement of Trp182 of 0.96 Å. The largest Cα displacement is 1.13 Å and occurs for Lys216 at Δt = 1.725 ms. In helix F the Cα atoms of residues 174 to 178 are displaced by only 0.4 Å and therefore, as with cryo-trapped structures of M-intermediates (*34-37*), TR-SFX does not reveal the large movements of helices E and F that were predicted from bR triple-mutant structures (*32, 38*). This discrepancy may be reconciled by noting that motions of these helices are severely restricted in the $P6_3$ crystal form because residues 165 and 166 of the E-F loop participate in crystal contacts with residues 232 and 234 of the C-terminus (fig. S7). Although larger motions of the CP portions of helices E and F arise later in the bR photocycle (*39, 40*) these structural changes cannot be critical for the mechanism of proton pumping because they are suppressed in 3D crystals yet the photocycle is similar to that of bR in the purple membrane (fig. S3) and the D96G/F171C/F219L bR triple mutant is constitutively open to the CP yet is able to pump protons (*41*).

Mechanistic overview

Retinal isomerization reorients the SB proton into a hydrophobic cavity while breaking its H-bond to Wat402, both of which lower the proton affinity of the SB (*14*). An initially twisted retinal becomes planar within 290 ns, causing Trp182 and Leu93 to be displaced towards the cytoplasm and allowing a water molecule to order between Leu93, Thr89 and the SB in the L-state. H-bond interactions from the protonated SB to Wat452 or Thr89 create a pathway for proton transfer to Asp85 (Fig. 4B) and explain how the SB makes contact with Asp85 despite been turned towards the CP by photo-isomerization. A steric clash between Cε of Lys216 and Wat402 dislodges this water molecule, triggering the collapse of the water mediated H-bond network on the EC side of bR. This allows helix C to bend towards helix G approximately 10 μs after photoactivation and raises the pKa of Asp85 to the point where it may spontaneously accept a proton from the SB. Once a proton is transferred, the Asp85-Thr89 H-bond is lost (Fig. 5D) which breaks the SB connectivity to the EC side of the protein. Consequently diffraction data spanning five orders of magnitude in time reveal how structural changes in bR achieve unidirectional membrane transport a half century after Jardetzky first proposed the alternating access framework obeyed by all membrane transporters (*1*).

CAPTIONS TO FIGURES:

Figure 1: Structure and function of bR. (**A**) Schematic illustrating retinal covalently bound to Lys216 through a protonated Schiff base in an all-*trans* and 13-*cis* configuration. (**B**) Proton exchange steps (arrows) achieving proton pumping by bR. The primary proton transfer step is from the SB to Asp85 and corresponds to the spectroscopic L to M transition. (**C**) $2mF_{obs}$-DF_{calc} electron density for the bR active site in its resting conformation. Electron density (grey) is contoured at ± 1.5 σ (σ is the root mean square electron density of the map).

Figure 2: Early structural changes in the bR photocycle. (**A**) View of the $|F_{obs}|^{light}–|F_{obs}|^{dark}$ difference Fourier electron density map near the retinal for Δt = 16 ns. Blue is positive difference electron density and yellow is negative difference electron density (contoured at ± 3.5 σ; σ is the root mean square electron density of the map). The resting state bR model (purple) was used for phases when calculating this map. Paired negative and positive difference electron densities indicate a sideways movement of the retinal's C20 methyl. (**B**) Identical representation but for the time-point Δt = 290 ns. (**C**) Crystallographic models deriving from partial occupancy refinement for Δt = 16 ns (blue) and Δt = 290 ns (red) superimposed upon the resting bR structure (purple, partially transparent).

Figure 3: Relative changes of electron density amplitudes in bR with time. (**A**) Time-dependent root mean square difference electron density amplitudes associated with Wat402 (blue), helix C (green, backbone of Arg82, Ala84 and Asp85), Waters 400, 401 and 451 (red, EC waters) and the side chain of Arg82 (purple). (**B**) Time-dependent amplitudes associated with the retinal (blue), the side chain of Lys216 (green), helix G (red, backbone of Ser214, Ala215 and Lys216) and helix F (purple, side-chains of Trp178 and Trp182 and backbone of Arg175). (**C**) Time-dependent amplitudes associated with Leu93 (blue), the side chain of Thr89 (green), Wat452 (red) and the side chain of Asp85 (purple). Amplitudes were averaged over the last four time-points and scaled to 1 (except Leu93, Wat452 (*42*)). Amplitudes for Δt = 95.2 µs, 657 µs and 1.725 ms are scaled by 2.0, 1.5 and 0.8 respectively (*42*). Linear decomposition of electron density amplitudes show how these motions are coordinated (fig. S8). The M-state population measured from microcrystalline slurries is indicated for comparison (dashed black line).

Figure 4: Pathway for proton transfer from the SB to Asp85. (**A**) View of the $|F_{obs}|^{light}-|F_{obs}|^{dark}$ difference Fourier electron density map (contoured at ± 3.0 σ) near the retinal for Δt = 760 ns. A positive difference feature (arrow) suggests the ordering of a water molecule (Wat452). (**B**) Crystallographic model for the time-point Δt = 760 ns (red) superimposed upon the resting state model (purple, partially transparent).

Figure 5: bR conformation controlling the primary proton transfer event. (**A**,**B**) View of the Difference Fourier electron density map immediately to the EC side of the retinal for (**A**) Δ*t* = 2 μs and (**B**) Δ*t* = 36.2 μs. All maps are contoured at 3.5 σ. Difference Fourier electron density maps from this viewpoint are shown for all thirteen time-points in Movie S2. (**C**) Crystallographic structural models deriving from partial occupancy refinement are superimposed upon the resting bR structure (purple, partially transparent) for Δ*t* = 16 ns (blue), 760 ns (red), 36.2 μs (orange) and 1.725 ms (yellow). (**D**) Close-up view of difference electron density across the Asp85-Thr89 H-bond for the time-points Δ*t* = 2 μs, 5.25 μs, 13.8 μs, 36.2 μs, 95.2 μs and 250 μs.

Figure 6: Conformational changes on the CP side of bR. (**A-B**) Close up view of the difference Fourier electron density map immediately to the CP side of the retinal for (**A**) Δ*t* = 760 ns and (**B**) Δ*t* = 1.725 ms. All maps are contoured at ± 3.5 σ. Difference Fourier electron density maps from this viewpoint are shown for all thirteen time-points in Movie S3. (**C**) Crystallographic structural models deriving from partial occupancy refinement are superimposed upon the resting bR structure (purple, partially transparent) for Δ*t* = 16 ns (blue), 760 ns (red), 36.2 μs (orange) and 1.725 ms (yellow).

REFERENCES

1. O. Jardetzky, Simple allosteric model for membrane pumps. *Nature* **211**, 969-970 (1966).

2. J. Tenboer *et al.*, Time-resolved serial crystallography captures high-resolution intermediates of photoactive yellow protein. *Science* **346**, 1242-1246 (2014).

3. T. R. Barends *et al.*, Direct observation of ultrafast collective motions in CO myoglobin upon ligand dissociation. *Science* **350**, 445-450 (2015).

4. K. Pande *et al.*, Femtosecond structural dynamics drives the trans/cis isomerization in photoactive yellow protein. *Science* **352**, 725-729 (2016).

5. U. Haupts, J. Tittor, D. Oesterhelt, Closing in on bacteriorhodopsin: progress in understanding the molecule. *Annu. Rev. Biophys. Biomol. Struct.* **28**, 367-399 (1999).

6. R. Neutze *et al.*, Bacteriorhodopsin: a high-resolution structural view of vectorial proton transport. *Biochim. Biophys. Acta* **1565**, 144-167 (2002).

7. C. Wickstrand, R. Dods, A. Royant, R. Neutze, Bacteriorhodopsin: Would the real structural intermediates please stand up? *Biochim. Biophys. Acta* **1850**, 536-553 (2015).

8. Y. Matsui *et al.*, Specific damage induced by X-ray radiation and structural changes in the primary photoreaction of bacteriorhodopsin. *J. Mol. Biol.* **324**, 469-481 (2002).

9. V. I. Borshchevskiy, E. S. Round, A. N. Popov, G. Buldt, V. I. Gordeliy, X-ray-radiation-induced changes in bacteriorhodopsin structure. *J. Mol. Biol.* **409**, 813-825 (2011).

10. V. Borshchevskiy *et al.*, Low-dose X-ray radiation induces structural alterations in

proteins. *Acta Crystallogr. D* **70**, 2675-2685 (2014).

11. R. Neutze, R. Wouts, D. van der Spoel, E. Weckert, J. Hajdu, Potential for biomolecular imaging with femtosecond X-ray pulses. *Nature* **406**, 752-757 (2000).

12. K. Hirata *et al.*, Determination of damage-free crystal structure of an X-ray-sensitive protein using an XFEL. *Nat. Meth.* **11**, 734-736 (2014).

13. H. Luecke, H. T. Richter, J. K. Lanyi, Proton transfer pathways in bacteriorhodopsin at 2.3 angstrom resolution. *Science* **280**, 1934-1937 (1998).

14. M. Sheves, A. Albeck, N. Friedman, M. Ottolenghi, Controlling the pKa of the bacteriorhodopsin Schiff base by use of artificial retinal analogues. *Proc. Natl. Acad. Sci. USA* **83**, 3262-3266 (1986).

15. C. H. Chang, R. Jonas, R. Govindjee, T. G. Ebrey, Regeneration of blue and purple membranes from deionized bleached membranes of *Halobacterium halobium*. *Photochem. Photobiol.* **47**, 261- 265. (1988).

16. S. E. Hayashi, E. Tajkhorshid, K. Schulten, Structural changes during the formation of early intermediates in the bacteriorhodopsin photocycle. *Biophys. J.* **83**, 1281-1297 (2002).

17. A. N. Bondar, S. Fischer, S. Suhai, J. C. Smith, Tuning of retinal twisting in bacteriorhodopsin controls the directionality of the early photocycle steps. *J. Phys. Chem. B* **109**, 14786-14788 (2005).

18. K. Edman *et al.*, High-resolution X-ray structure of an early intermediate in the bacteriorhodopsin photocycle. *Nature* **401**, 822-826 (1999).

19. K. Nass *et al.*, Indications of radiation damage in ferredoxin microcrystals using high-intensity X-FEL beams. *J. Synch. Rad.* **22**, 225-238 (2015).

20. B. Schobert, J. Cupp-Vickery, V. Hornak, S. Smith, J. Lanyi, Crystallographic structure of the K intermediate of bacteriorhodopsin: conservation of free energy after photoisomerization of the retinal. *J. Mol. Biol.* **321**, 715-726 (2002).

21. H. G. Khorana, Two light-transducing membrane proteins: bacteriorhodopsin and the mammalian rhodopsin. *Proc. Natl. Acad. Sci. USA* **90**, 1166-1171 (1993).

22. G. A. Jeffrey, *An introduction to hydrogen bonding*. (Oxford University Press, 1997).

23. T. Kouyama, T. Nishikawa, T. Tokuhisa, H. Okumura, Crystal structure of the L intermediate of bacteriorhodopsin: evidence for vertical translocation of a water molecule during the proton pumping cycle. *J. Mol. Biol.* **335**, 531-546 (2004).

24. A. Royant *et al.*, Helix deformation is coupled to vectorial proton transport in the photocycle of bacteriorhodopsin. *Nature* **406**, 645-648 (2000).

25. K. Edman *et al.*, Deformation of helix C in the low temperature L-intermediate of bacteriorhodopsin. *J. Biol. Chem.* **279**, 2147-2158 (2004).

26. J. K. Lanyi, B. Schobert, Structural changes in the L photointermediate of bacteriorhodopsin. *J. Mol. Biol.* **365**, 1379-1392 (2007).

27. A. Maeda *et al.*, Interaction of internal water molecules with the schiff base in the L intermediate of the bacteriorhodopsin photocycle. *Biochemistry* **41**, 3803-3809 (2002).

28. A. Maeda, F. L. Tomson, R. B. Gennis, S. P. Balashov, T. G. Ebrey, Water molecule rearrangements around Leu93 and Trp182 in the formation of the L intermediate in bacteriorhodopsin's photocycle. *Biochemistry* **42**, 2535-2541 (2003).

29. A. N. Bondar, J. Baudry, S. Suhai, S. Fischer, J. C. Smith, Key role of active-site water molecules in bacteriorhodopsin proton-transfer reactions. *J. Phys. Chem. B* **112**, 14729-14741 (2008).

30. A. Maeda *et al.*, Water-mediated hydrogen-bonded network on the cytoplasmic side of the Schiff base of the L photointermediate of bacteriorhodopsin. *Biochemistry* **42**, 14122-14129 (2003).

31. R. Pomes, B. Roux, Structure and dynamics of a proton wire: a theoretical study of H+ translocation along the single-file water chain in the gramicidin A channel. *Biophys J* **71**, 19-39 (1996).

32. S. Subramaniam, R. & Henderson, Molecular mechanism of vectorial proton translocation by bacteriorhodopsin. *Nature* **406**, 653-657 (2000).

33. H. Kandori *et al.*, Tight Asp-85--Thr-89 association during the pump switch of bacteriorhodopsin. *Proc Natl Acad Sci U S A* **98**, 1571-1576 (2001).

34. H. Luecke, B. Schobert, H. T. Richter, J. P. Cartailler, J. K. & Lanyi, Structural changes

in bacteriorhodopsin during ion transport at 2 angstrom resolution. *Science* **286**, 255-261 (1999).

35. H. Luecke *et al.*, Coupling photoisomerization of retinal to directional transport in bacteriorhodopsin. *J. Mol. Biol.* **300**, 1237-1255 (2000).

36. H. J. Sass *et al.*, Structural alterations for proton translocation in the M state of wild-type bacteriorhodopsin. *Nature* **406**, 649-653 (2000).

37. M. T. Facciotti *et al.*, Structure of an early intermediate in the M-state phase of the bacteriorhodopsin photocycle. *Biophys J* **81**, 3442-3455 (2001).

38. T. Wang *et al.*, Deprotonation of D96 in bacteriorhodopsin opens the proton uptake pathway. *Structure* **21**, 290-297 (2013).

39. M. H. Koch *et al.*, Time-resolved X-ray diffraction study of structural changes associated with the photocycle of bacteriorhodopsin. *EMBO J* **10**, 521-526 (1991).

40. M. Andersson *et al.*, Structural dynamics of light-driven proton pumps. *Structure* **17**, 1265-1275 (2009).

41. J. Tittor *et al.*, Proton translocation by bacteriorhodopsin in the absence of substantial conformational changes. *J Mol Biol* **319**, 555-565 (2002).

42. See online materials and methods. .

43. E. M. Landau, J. P. Rosenbusch, Lipidic cubic phases: a novel concept for the crystallization of membrane proteins. *Proc Natl Acad Sci U S A* **93**, 14532-14535 (1996).

44. P. Nollert, Lipidic cubic phases as matrices for membrane protein crystallization. *Methods* **34**, 348-353 (2004).

45. K. Tono *et al.*, Beamline, experimental stations and photon beam diagnostics for the hard x-ray free electron laser of SACLA. *New J. Phys.* **15**, 083035 (2013).

46. K. Tono *et al.*, Diverse application platform for hard X-ray diffraction in SACLA (DAPHNIS): application to serial protein crystallography using an X-ray free-electron laser. *J. Synchrotron Rad.* **22**, 532-537 (2015).

47. U. Weierstall *et al.*, Lipidic cubic phase injector facilitates membrane protein serial femtosecond crystallography. *Nat Commun* **5**, 3309 (2014).

48. P. Nogly *et al.*, Lipidic cubic phase injector is a viable crystal delivery system for time-resolved serial crystallography. *Nat Commun* **7**, 12314 (2016).

49. T. Kameshima *et al.*, Development of an X-ray pixel detector with multi-port charge-coupled device for X-ray free-electron laser experiments. *Rev Sci Instrum* **85**, 033110 (2014).

50. T. Nakane *et al.*, Data processing pipeline for serial femtosecond crystallography at SACLA. *J. Appl. Crystallogr.* **49**, 1035-1041 (2016).

51. A. Barty *et al.*, Cheetah: software for high-throughput reduction and analysis of serial femtosecond X-ray diffraction data. *J. Appl. Crystallogr.* **47**, 1118-1131 (2014).

52. T. a. White *et al.*, CrystFEL : a software suite for snapshot serial crystallography. *J. Appl.*

Crystallogr. **45**, 335-341 (2012).

53. S. Zaefferer, New developments of computer-aided crystallographic analysis in transmission electron microscopy. *J. Appl. Crystallogr.* **33**, 10-25 (2000).

54. A. Duisenberg, Indexing in single-crystal diffractometry with an obstinate list of reflections. . *J. Appl. Crystallogr.* **25**, 92-96 (1992).

55. T. A. White *et al.*, Crystallographic data processing for free-electron laser sources. *Acta Crystallogr. D* **69**, 1231-1240 (2013).

56. M. D. Winn *et al.*, Overview of the CCP4 suite and current developments. *Acta Crystallogr. D* **67**, 235-242 (2011).

57. P. R. Evans, An introduction to data reduction: space-group determination, scaling and intensity statistics. *Acta Crystallogr. D* **67**, 282-292 (2011).

58. R. H. Blessing, G. D. Smith, Difference structure-factor normalization for heavy-atom or anomalous-scattering substructure determinations. *J. Appl. Crystallogr.* **32**, 664-670 (1999).

59. L. Ten, Crystallographic fast Fourier transforms. *Acta Crystallogr. A* **29**, 183-191 (1973).

60. R. C. TeamR. (R foundation for Statistical Computing, Vienna, Austria, 2013).

61. M. Schmidt, S. Rajagopal, Z. Ren, K. Moffat, Application of singular value decomposition to the analysis of time-resolved macromolecular x-ray data. *Biophys J* **84**, 2112-2129 (2003).

62. A. Vagin, A. Teplyakov, MOLREP: an Automated Program for Molecular Replacement. *J. Appl. Crystallogr.* **30**, 1022-1025 (1997).

63. P. Emsley, K. Cowtan, Coot: model-building tools for molecular graphics. *Acta Crystallogr. D* **60**, 2126-2132 (2004).

64. A. A. Vagin *et al.*, REFMAC5 dictionary: organization of prior chemical knowledge and guidelines for its use. *Acta Crystallogr. D* **60**, 2184-2195 (2004).

65. P. D. Adams *et al.*, PHENIX: building new software for automated crystallographic structure determination. *Acta Crystallogr. D* **58**, 1948-1954 (2002).

66. B. R. Brooks *et al.*, CHARMM: a program for macromolecular energy, minimization, and dynamics calculations. *J. Comput. Chem* **4**, 187-217 (1983).

67. G. Metz, F. Siebert, M. Engelhardt, Asp85 is the only internal aspartic acid that gets protonated in the M intermediate and the purple-to-blue transition of bacteriorhodopsin. A solid-state 13C CP-MAS NMR investigation. *FEBS Lett.* **303**, 237-241 (1992).

68. L. S. Brown *et al.*, Glutamic acid 204 is the terminal release group at the extracellular surface of bacteriorhodopsin. *J. Biol. Chem.* **270**, 27122-27126 (1995).

69. P. H. König, M. Hoffmann, T. Frauenheim, Q. Cui, A critical evaluation of different QM/MM frontier treatments with SCC-DFTB as the QM method. *J. Phys. Chem. B* **109**, 9082-9095 (2005).

70. M. Elstner *et al.*, Self-consistent-charge-density-functional tight-binding method for

simulations of complex material properties. *Phys. Rev. B* **58**, 7260-7268 (1998).

71. Q. Cui, M. Elstner, E. Kaxiras, T. Frauenheim, M. Karplus, A QM/MM implementation of the Self-Consistent Charge Density Functional Tight Binding (SCC-DFTB) method. *J. Phys. Chem. B* **105**, 569-585 (2001).

72. M. Gaus, Q. Cui, M. Elstner, DFTB3: extension of the self-consistent charge-density functional tight-binding method (SCC-DFTB). *J. Chem. Theory Comput.* **7**, 931-948 (2011).

73. M. Gaus, A. Goez, M. Elstner, Parametrization and benchmark of DFTB3 for organic molecules. *J. Chem. Theory Comput.* **9**, 338-354 (2013).

74. A. D. MacKerell *et al.*, All-atom empirical potential for molecular modeling and dynamics studies of proteins. *J Phys Chem B* **102**, 3586-3616 (1998).

75. A. D. MacKerell Jr., M. Feig, C. L. I. Brooks, Extending the treatment of backbone energetics in protein force fields: limitations of gas-phase quantum mechanics in reproducing protein conformational distributions in molecular dynamics simulations. *J. Comput. Chem* **25**, 1400-1415 (2004).

76. W. L. Jorgensen, J. Chandrasekhar, J. D. Madura, R. W. Impey, M. L. Klein, Comparison of simple potential functions for simulating liquid water. *J. Chem. Phys.* **79**, 926-935 (1983).

Acknowledgements: We thank Ms. Oshimo for her help in culturing *H. salinarum* and members of the Engineering Team of RIKEN SPring-8 Center, especially Mr. Shimazu, Mr. Hata, Mr. Suzuki and Mr. Kin, for technical support. XFEL experiments were conducted at BL3 of SACLA with the approval of the Japan Synchrotron Radiation Research Institute (JASRI) (Proposal Numbers 2014B8051, 2015A8047 and 2015B8054). Crystals were checked for diffraction at BL41XU of SPring-8 with the approval of the JASRI (Proposal Numbers 2015A1119). This work was supported by the X-ray Free-Electron Laser Priority Strategy Program (MEXT) and partially by the Strategic Basic Research Program (JST) and RIKEN Pioneering Project Dynamic Structural Biology. We acknowledge computational support from SACLA HPC system and Mini-K super computer system. R.N. acknowledges financial support from the Swedish Research Council (VR 349-2011-6485 and 2015-00560), the Swedish Foundation for Strategic Research (SSF SRL 10-0036) and the Knut and Alice Wallenberg Foundation (KAW 2012.0284). AR acknowledges financial support from the French National Research Agency (Grant number: ANR-11-JSV5-0009). T. Kimura is supported by JSPS KAKENHI Grant Number 15H05476. P.N. acknowledges support from the European Community's Seventh Framework Program (FP7/2007-2013) under grant agreement n.°290605 (PSI-FELLOW/COFUND). J.S. acknowledges support from the Swiss National Science Foundation project grant (SNF 31003A_159558). G.S. acknowledges support from the Swiss National Science Foundation (grant SNF

310030_153145 and NCCR-MUST/FAST). C.S. is supported by NRF through the SRC (NRF-2015R1A5A1009962) and the POSCO Green Science program. A.-N.B. acknowledges support in part from the Excellence Initiative of the German Federal and State Governments provided via the Freie Universität Berlin, the Deutsche Forschungsgemeinschaft, DFG, Collaborative Research Center SFB1078 project C4, and computing time from the Freie Universität Berlin and from the HLRN, the North-German Supercomputing Alliance. M.M. acknowledges financial support from the Exploratory Research for Advanced Technology of the JST. The authors have made the following contributions: S.I., R.N. and E.N. conceived the research; T.T., T.A., A.Y., J.K., R.T., E.N., P.N., J.S. prepared microcrystals; S.M., S.K. and M.M. prepared purple membrane; E.N., C.S., R.N., M.K. and K.T. designed the experimental setup; M.K., T.Kimura, T.Nomura, S.O. and J.D. contributed the pump laser setup; E.N., T.T., R.T., T.A., A.Y., J.K., T.Hosaka., E.M., P.N., M.S., C.S. D.N., R.D., Y.K., T.S., D.I., T.F., Y.Y., B.J., T.Nishizawa, K.O., M.F., C.W., R.A., C.S., P.B., J.S. and R.N. performed data collection; M.K., T.Kimura and T.Nomura performed time-resolved visible absorption spectroscopy and C.W. and R.N. analyzed the spectral data; T.Nakane and O.N. performed data processing; A.R. and E.N. refined the intermediate structures; A.-N.B. performed computations; K.T., C.S., T.Kameshima, T.Hatsui., Y.J. and M.Y. developed the SFX systems at SACLA; and R.N., C.W., E.N., A.R. M.K. and T.Nakane wrote the

paper with input from all authors. Coordinates and structure factors have been deposited in the Protein Data Bank with accession numbers: 5B6V (bR resting state); 5B6W (Δt = 16 ns); 5H2H (Δt = 40 ns); 5H2I (Δt = 110 ns); 5H2J (Δt = 290 ns); 5B6X (Δt = 760 ns); 5H2K (Δt = 2 μs); 5H2L (Δt = 5.25 μs); 5H2M (Δt = 13.8 μs); 5B6Y (Δt = 36.2 μs); 5H2N (Δt = 95.2 μs); 5H2O (Δt = 250 μs); 5H2P (Δt = 657 μs); and 5B6Z (Δt = 1.725 ms). Raw diffraction images have been deposited in the CXIDB (accession ID 53).

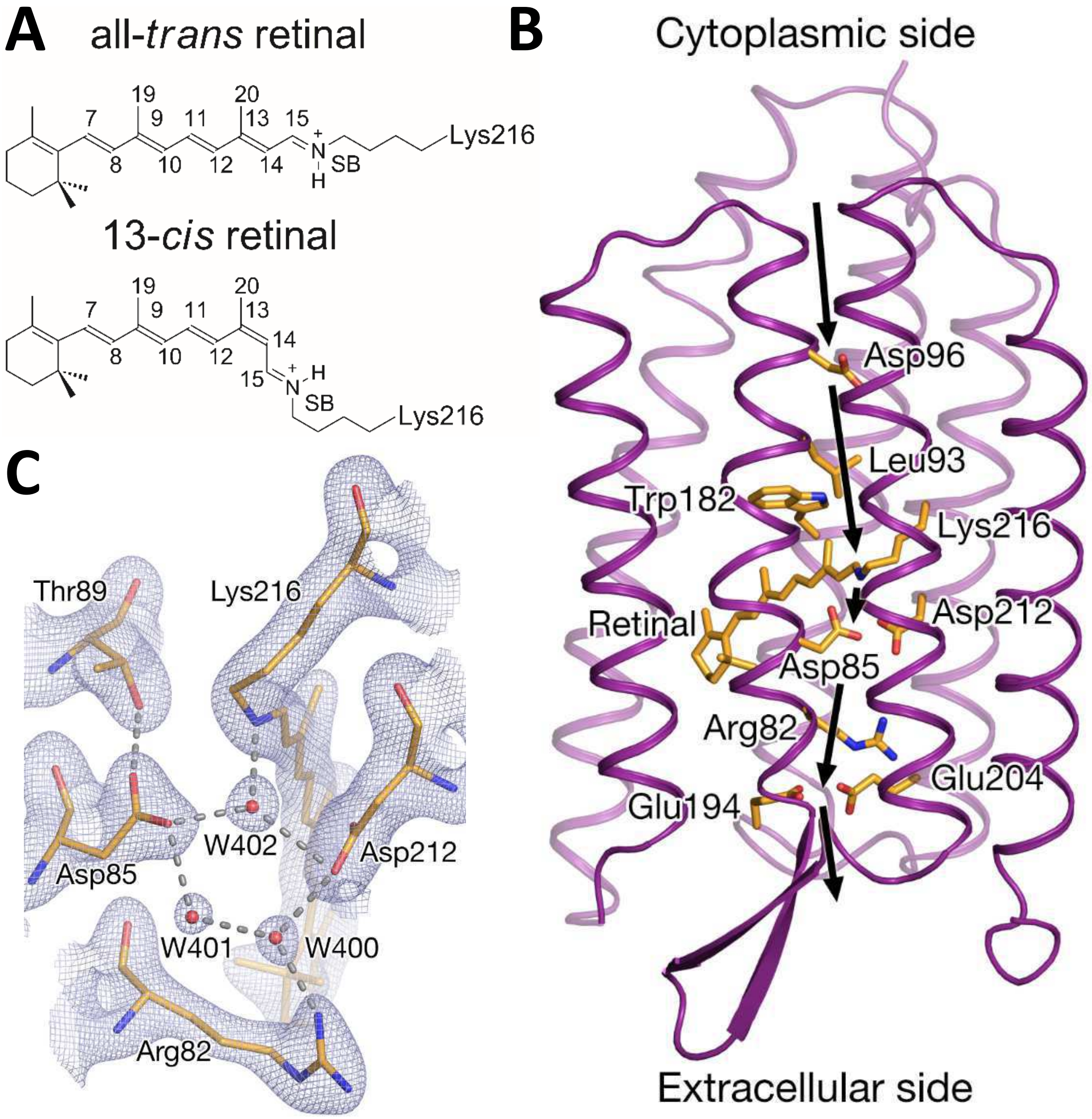

Figure 1: Nango *et al.*

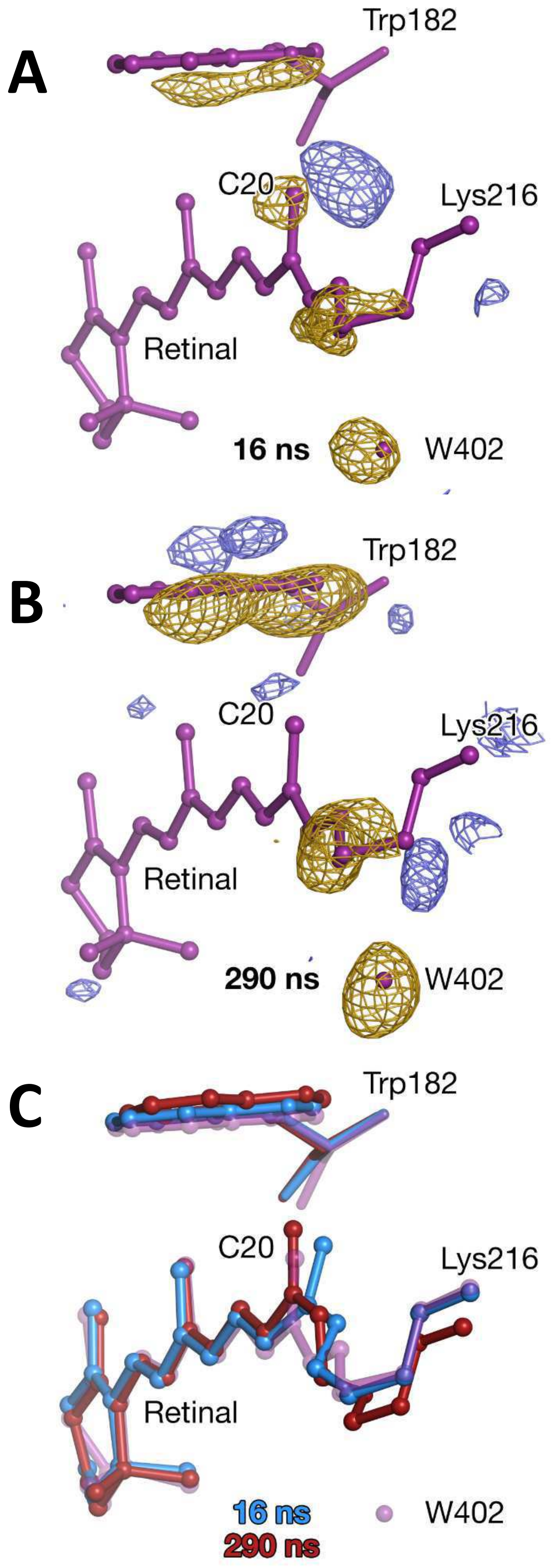

Figure 2: Nango *et al.*

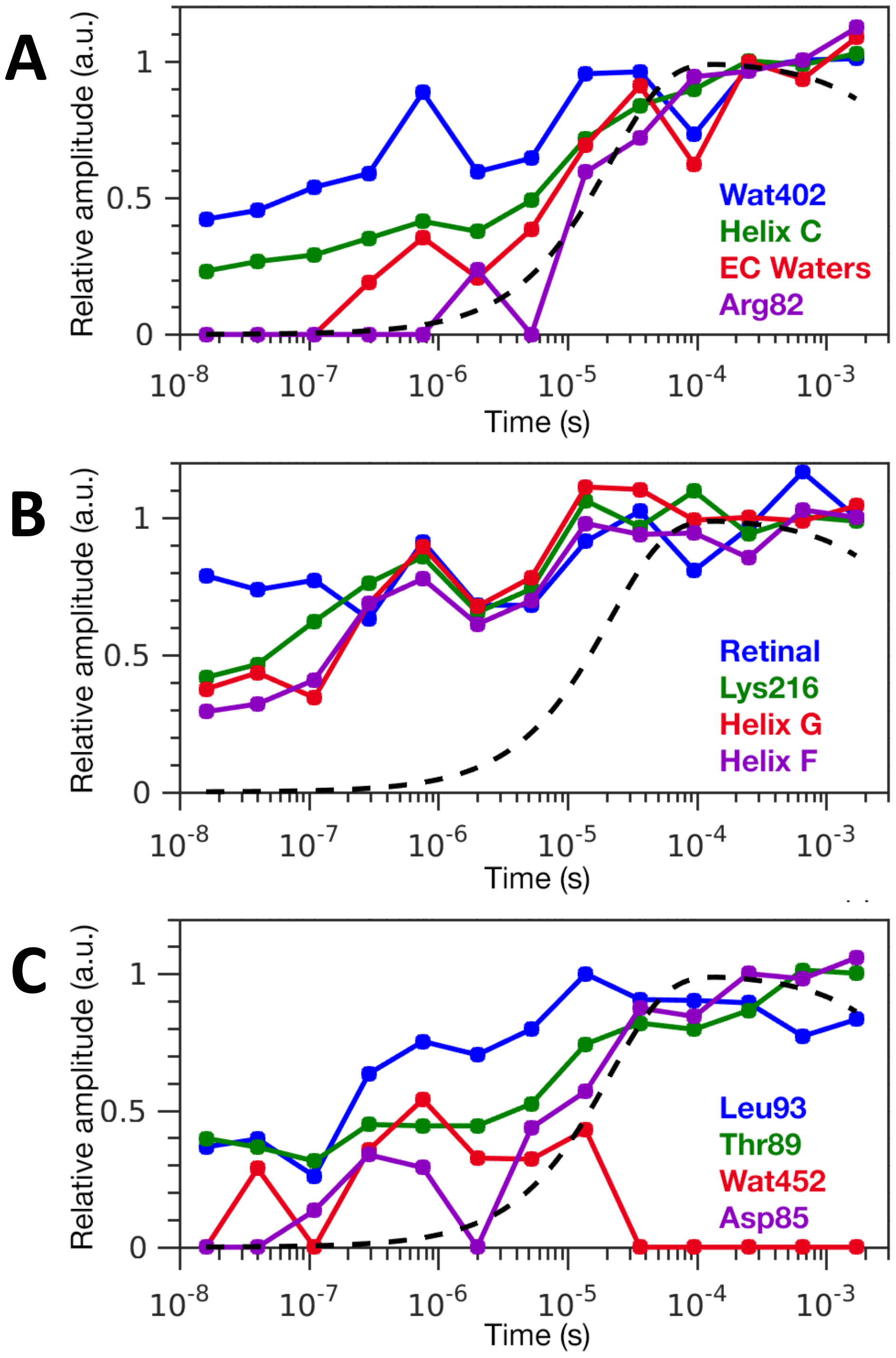

Figure 3: Nango *et al.*

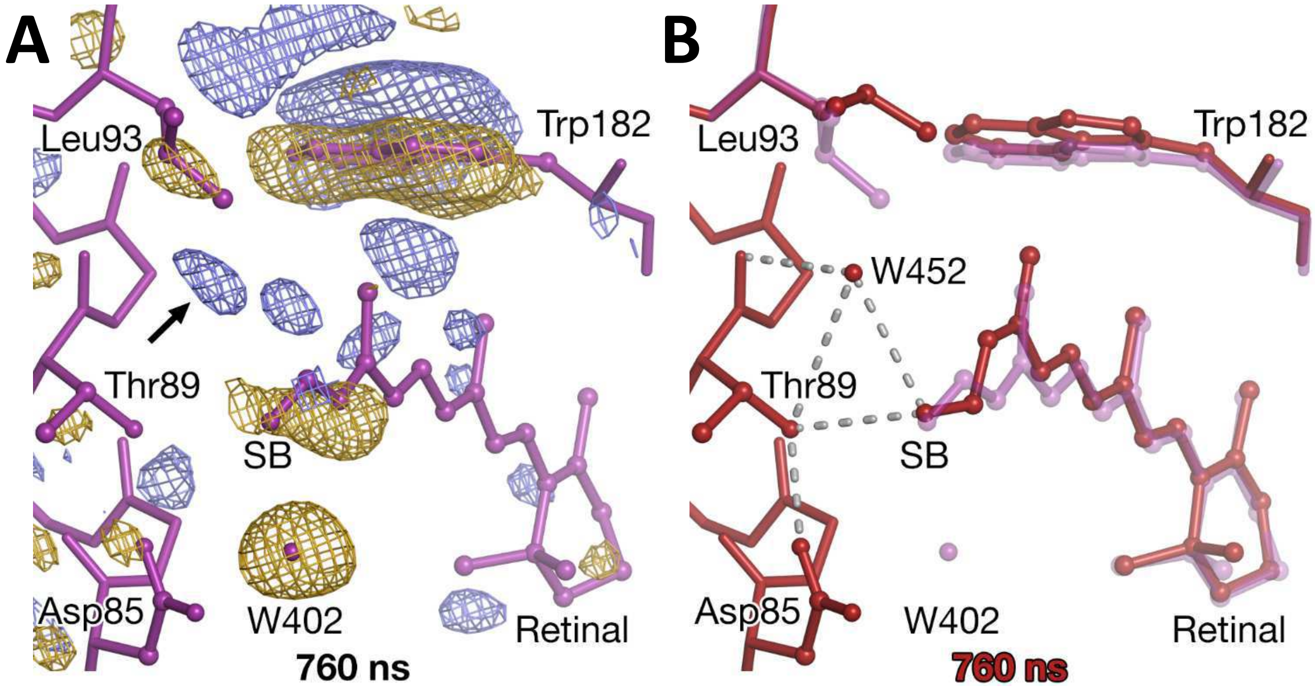

Figure 4: Nango *et al.*

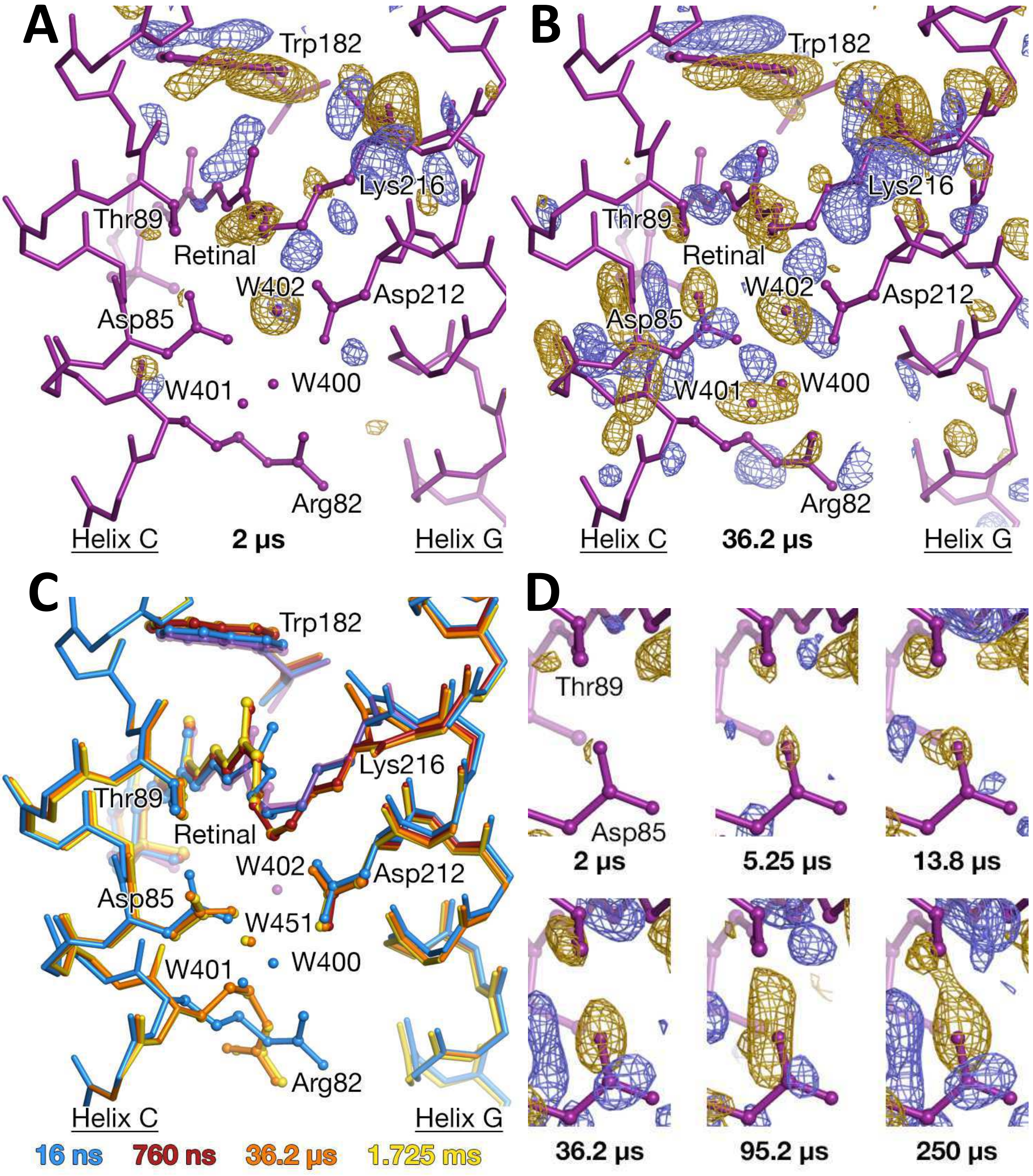

Figure 5: Nango *et al.*

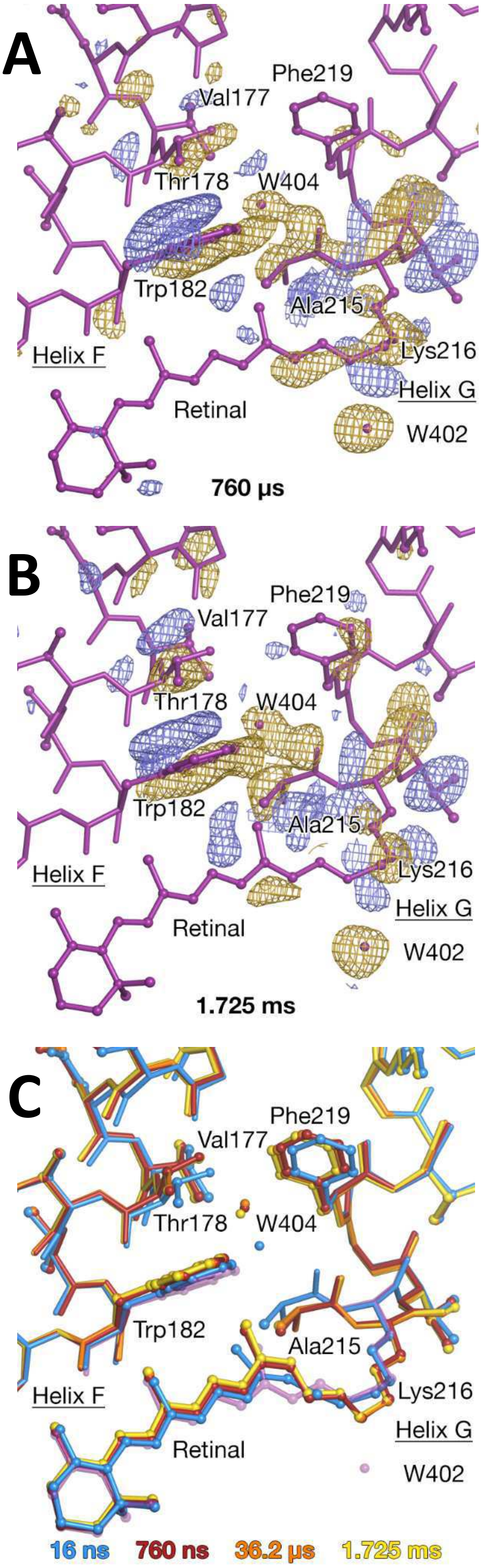

Figure 6: Nango *et al.*